Proceedings of ASME Turbo Expo 2011
GT2011
June 6-10, 2011, Vancouver, British Columbia, Canada

GT2011-46119

INVESTIGATION OF PRE-STALL BEHAVIOR IN AN AXIAL COMPRESSOR ROTOR-PART 1: UNSTEADINESS OF TIP CLEARANCE FLOW

Yanhui Wu, Qingpeng Li, Jiangtao Tian, Wuli Chu
School of Power and Energy, Northwestern Polytechnical University
Xi'an, Shanxi, P.R. China

ABSTRACT

In order to investigate the pre-stall behavior of an axial flow compressor rotor, which was experimentally observed with spike-type stall inception, systematical experimental and whole-passage simulations were laid out to analyze the internal flow fields in the test rotor. In this part, emphases were put on the analyses of experimental results and the predicted results from steady simulations and unsteady simulations, which converged to equilibrium solutions with nearly periodic fluctuations of efficiency. The objective was to uncover the unsteady behavior of tip clearance flow and its associated flow mechanism at near stall conditions.

To validate the steady simulation results, the predicted total characteristics and spanwise distributions of aerodynamic parameters were first compared with the measured steady data, and a good agreement was achieved. Then, the numerically obtained unsteady flowfields during one period of efficiency fluctuations were analyzed in detail. The instantaneous flow structure near casing showed that tip secondary vortex (TSV), which appeared in the previous unsteady single-passage simulations, did exist in tip flowfields of whole-passage simulations. The cyclical motion of this vortex was the main source of the nearly periodic variation of efficiency. The simulated active period of TSV increased with the mass flow rate decreased. The simulated frequency of TSV at flow condition very close to the measured stall point equaled to the frequency of the characteristic hump identified from the instantaneous casing pressure measurements. This coincidence implied the occurrence of this hump was most probably due to the movement of TSV.

Further flowfield analyses indicated the interaction of the low-energy leakage fluid from adjacent passages with the broken-downed TLV was the flow mechanism for the formation of TSV. Once TSV appeared in tip flowfields, its rearward movement would lead to a periodic variation in near-tip blade loading, which in turn altered the strength of TLV and TSV, accordingly the low-energy regions associated with the breakdown of TLV and the motion of TSV, thus establishing a self-sustained unsteady flow oscillation in tip flowfields.

INTRODUCTION

It is well known that tip clearance flow and its associated vortex affect the performance and stability of axial flow compressors. Therefore, much effort was made to explore the flow mechanism of tip clearance flow and it possible link with stall inception process in axial compressors. Inoue et al. [1-2] measured tip leakage flow fields behind and inside a low-speed compressor rotor at design condition. They found the interaction between tip leakage flow and incoming flow forced tip leakage flow rolling up into a slender vortex, which can be clearly seen a coiling of secondary vectors near the casing. However, when they conducted measurement on the same test rig [3, 4] at near stall condition, the abnormal flow phenomena were observed: the coiling of secondary vectors near the casing disappeared, while the low-energy fluid were spread out to about 60% percent of span. This inexplicable behavior of tip leakage vortex remained an unresolved puzzle during that period. Benefiting from the development of CFD techniques, Furukawa et al. [5] proposed a reasonable interpretation of the above abnormal phenomena from a viewpoint of "vortex breakdown" through analyzing the simulated flow field in detail. Besides, Bialjie et al [6] showed the evidence of the breakdown of tip leakage vortex based on SPIV measurements in a low-speed large scale axial flow compressor test rig.

When compressors approach the stall limit, the unsteadiness of flow fields near casing became more and more dominant. Furukawa et al. [7] and Yamada et al [8] numerically investigated unsteady behaviors in a low-seed and a transonic axial compressor rotor. They found the breakdown of tip leakage vortex was responsible for the unsteadiness of flow fields near the casing. However, experimental and numerical investigations conducted by März et al. [9] revealed that a vortex structure formed near the leading edge plane, which was the result of interactions among the classical tip-clearance flow, axially reverse end-wall flow, and incoming flow. The formation and movement of this vortex seemed to be the main causes of unsteadiness when the test low-speed compressor operated at near stall conditions.

Besides, efforts on understanding the onset of rotating stall/surge have been another research subject with the rapid advance of computer and CFD technology. Recent unsteady simulations to stall have achieved many valuable findings of flow structure leading to stall. Hoying et al. [10] first successfully simulated the short length-scale (or spike) rotating stall inception for the low-speed version of E^3 compressor. They found that the stall inception is a result of the motion of tip clearance vortex moving upstream of the blade passage when the vortex trajectory was aligned with the blade leading edge plane. Though systematical singe-passage and multi-passage simulations, Vo et al. [11] further proposed two conditions necessary for the formation of spike disturbance: one is that the spillage of tip clearance flow to the adjacent blade passage ahead of the rotor leading edge and below the blade tip; the other is the initiation of backflow stemming from the leakage fluid in adjacent passages at the trailing edge plane. Hereafter, the two necessary conditions will be referred as "tip clearance spillage flow" and "tip clearance backflow". It should be noted that the sequence of these two threshold event may alter, but both must be present for compressors exhibiting spike disturbances. Hah et al. [12] conducted full-annulus computations to investigate the short length-scale stall inception in a transonic axial compressor rotor, and their observations were consistent with the two condition proposed by Vo et al. [11]. Furthermore, Chen et al. [13] carried out the full-annulus calculations using high-performance parallel computing to study the pre-stall behavior of a transonic axial compressor stage. Their simulations demonstrated the development of the rotating stall from the growth of rotating instabilities, i.e., a rotating long-length disturbance followed by a spike-type breakdown. Further flow field analysis indicated that the spike instabilities occurred when the trajectory of tip clearance flow is vertical to the axial direction.

The above investigations just focus on the description of flow phenomena associated with spiked initiated rotating stall: the so-called "tip clearance spillage flow" and "tip clearance backflow". No attempts were made to explore the exact flow mechanism underlying these phenomena. It is no doubt that the instantaneous complicated flow structures near casing at near stall condition are closely related to the onset of rotating stall for tip critical compressors. Expressed in another way, what is the flow mechanism of unsteadiness of tip clearance flow at near stall conditions, and how it links with the spike disturbances emerging from the flow fields? This is the motivation for the current study.

The current study is based on a high-speed small-scale axial compressor rotor, which had been experimentally observed to exhibit the spike type stall inception. In order to get the answer of the above questions, the work reported here divide into two parts. Part I presented the experimental and whole-passage numerical investigations, and the aim was to uncover the flow mechanism of unsteadiness of tip clearance flow at near stall conditions. Based on the results from Part I, whole-passage unsteady simulation beyond the last stable point in Part I was further analyzed in Part II, and the objective was to explore the linkage between the unsteady nature of tip clearance flow and the spike emergence, i.e., the flow mechanism of spike emergence.

EXPERIMENTAL STUDY

Test Facility and Instrumentation

The present work was performed on the isolated axial compressor rotor test rig in Northwestern Polytechnical University at Xi'an. Figure 1 showed a cross-sectional diagram of this stand. It consisted of a DC motor (250 KW), an accelerator or gearbox, a torque meter, a test section, an orifice plate flow meter, a discharge duct, and a throttle cone. The test rotor was isolated from the stator to avoid interaction effects generated by the presence of a downstream stator blade row.

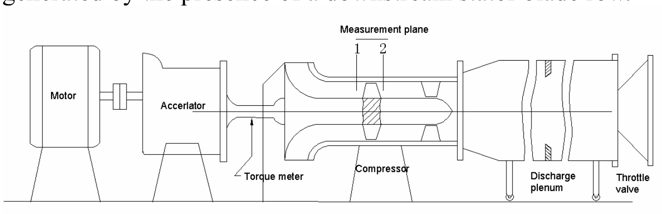

Figure 1 Cross-sectional diagram of the test rig.

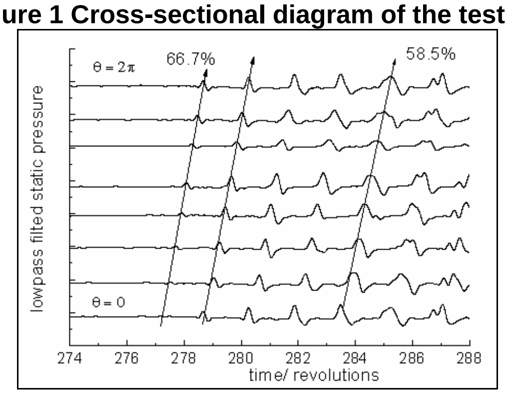

Figure 2 Typical stalling pattern of the test rotor

The hub/tip ratio of the rotor is 0.6, with the blade tip diameter of 298 mm. The rotor blade has Russia K70 series profile sections. The blade tip section of the rotor has the solidity of 0.961 and chord length of 30 mm. The nominal tip clearance is 0.3 mm (1.0 percent tip chord or 0.52 percent blade height), and it can be varied by exchanging casing segments with the rotor diameter remaining constant. Details of design specifications can refer to Xingen et al. [14]. Due to its tip critical nature, this rig has been widely used to test various kinds of casing treatment to determine their effectiveness on stall margin improvement (for example, Xingeng Lu et al. [14] Yanhui Wu et al. [15]). Recently, Lu [16] arranged 8 high-response pressure transducers ahead of rotor tip leading edge to detect pressure fluctuations during instability onset with steady-state clean inlet. The measurements were conducted at corrected rotor speed of 8130 rpm with two different clearance gaps of 1.0%, and 1.7% tip chord (or 0.52%, and 0.86% blade height). At all tested cases, the stalling pattern of the test rotor was similar, and the compressor showed a spike-type stall inception. Figure 2 illustrated the stalling pattern of the test rotor with the tip gap of 0.86% blade height. The propagation velocity of spike was about 66.7% rotor speed at beginning. and then quickly transitioned into rotating stall cell within about 3 rotor revolutions, and the final speed of rotating stall cell was about 58.5%.

However, the fundamental flow mechanisms that lead to stall inception are not well understood by measurements due to the small-scale of this rig. A series of computational investigations, including steady and unsteady numerical simulations, has been therefore laid out to achieve this goal. Yanhui wu et al. [17] conducted steady single-passage simulations for this test rotor. After validating simulation results with available experimental data, the numerically obtained flowfields were analyzed to identify the behavior of tip leakage flow. It was found that the breakdown of the leakage vortex occurred inside the rotor passage at near stall conditions. Due to the vortex breakdown, a low-velocity region developed along the vortex core, thus producing a large blockage effect on incoming flow near the pressure side of the passage. Sparked by the numerical investigations conducted by Vo [11], the similar single-passage unsteady computations were further carried out by Yanhui wu [18] to assess the unsteady behavior of tip clearance flow, and to identify the threshold flow event leading to the spike initiated rotating stall. It was found that the “tip clearance spillage flow” did occur, but there was no “tip clearance backflow” during the stall inception process. The most predominant feature of flow fields near casing was that there was another distinctive vortex appeared at near stall conditions, apart from the breakdown of leakage vortex. This vortex, denoted as tip secondary vortex (TSV) probably arose from the interaction of the tip clearance flow among the adjacent blade passages. Due to the formation and movement of this vortex, the substantial unsteadiness of tip clearance flow occurred. In these simulations, the corrected rotor speed and the tip clearance size were set to be 8130 rpm and 1.7% tip chord, which were identical to those in Figure 1.

Did the single-passage unsteady simulation really provide the useful information for spike-initiated stall despite of its periodic assumption along circumferential direction? The current experimental investigations thus laid out the steady and instantaneous measurements with the same corrected rotor speed and tip gap size as those used in the previous numerical investigations. The tests were conducted with clean inlet to assure undisturbed circumferential uniform flow to rotor, and the equivalent tip Mach number was about 0.41. On the one hand, steady measurements can provide comparison baselines for the current computational investigations. One the other hand, the instantaneous pressure signals at near stall conditions were measured based on the operating points determined by steady measurements.

The pressure ratio of the rotor were acquired using conventional static and total pressure combined probes, which were traversed radially approximately 50% axial-chord upstream of the rotor and 40% axial chord downstream of the rotor. Shaft speed and torque were measured by a torque meter device. The mass flow was measured using a calibrated orifice plate installed in the discharge plenum. Mass flow rate through the rotor can be varied by linear movement of a cone at the end of the constant area duct as shown in Figure 1. The measurement uncertainties are mass flow, ±0.1 kg/s; inlet total pressure, ±100 N/m2; outlet total pressure, ±300 N/m2; flow angle: ±2 Deg. Because the temperature rise across the rotor was very small, the efficiency was derived from the torque and mass flow with an iterative calculation process. Errors in calculated efficiency are estimated at ±0.8% maximum, as far as relative comparison between the results for each case is concerned. The stability limit was readily detected audibly as well as on pressure measuring instrumentation which indicated considerable unsteadiness. The limiting flow rates indicated are the “last” stable point that could be obtained before this instability.

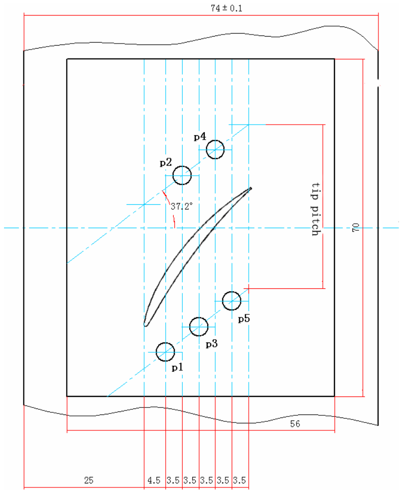

Figure 3 The arrangement of pressure transducers

To obtain the instantaneous pressure signals at near stall conditions, five high response frequency transducers (Kulite XCQ-080) were arranged on the casing as shown in Figure 3. Their respective locations away from the tip leading edge were 20, 36, 52, 68, and 84% tip chord. 5 channels were acquired simultaneously at 100 kHz. This sample rate resulted in 24 pressure samples per blade passage at corrected rotor speed of 8130 rpm, and sampling 60 seconds of time data was stored on the disk.

Measured Signal Characteristics

The instantaneous pressures on casing were acquired from peak efficiency point to stall point, which were indicated by **PE** and **SP** in Figure 8 respectively. To improve the resolution for the signal concerned, the original pressure signals were decomposed into five orders by virtue of db1 wavelet transformation shown in Figure 4. Then, the spectrum analyses aiming to the low-frequency-band signals of d5, d4 were conducted. A rather weak characteristic hump with frequency approximate to the simulated frequency of TSV firstly appeared at a near stall point, which was marked with **NSP1** in Figure 8. The energy of this characteristic hump increased as the operating point reached the stall point.

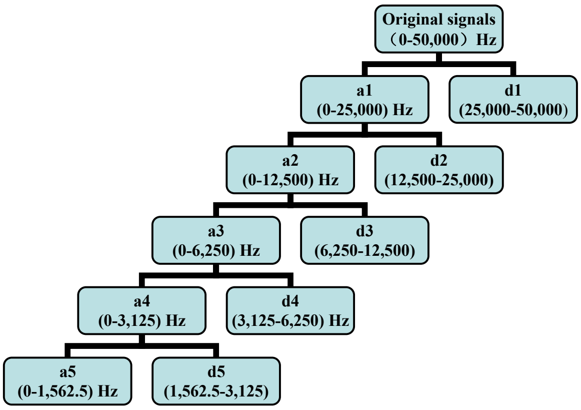

Figure 4 db1 transformations for original signals

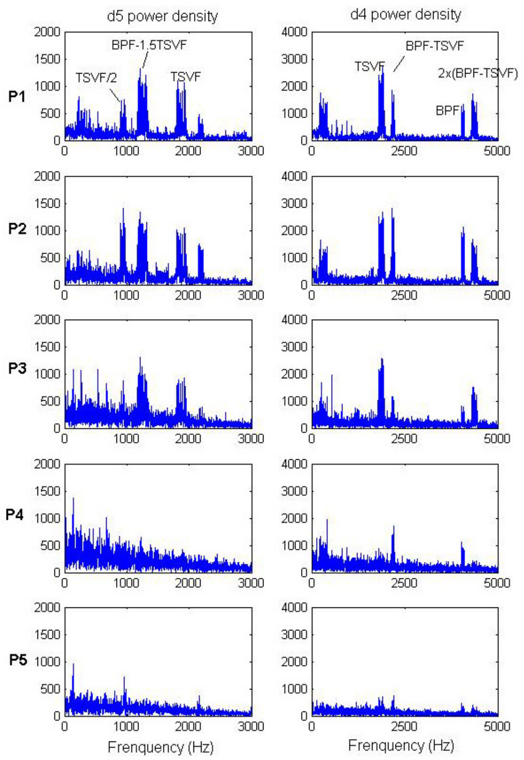

Figure 5 The power density aiming to the low-frequency-band signals of d5, d4 at last stable point from measurements.

Figure 5 presented the power density spectrums for d5 and d4 at stall point (SP). The first characteristic frequency identified was blade passing frequency (BPF). Another characteristic hump, which bandwidth varied between 1800 Hz and 1950 Hz, was clearly identified on d5 frequency-band. According to the simulation results observed by Yanhui et al. [18], the exact active frequency of TSV was 1694 Hz. The proximity of TSV frequency to the identified characteristic hump implied the appearance of this hump probably attributed to the activity of TSV, hence marking it with TSVF in Figure 5. Because all pressure signals were sampled at absolute frame, whereas the activity of TSV existed in relative frame. Due to the coordinate transform, other derivative frequencies, such as TSVF/2, BPF-1.5TSVF, BPF-TSVF, 2(BPF-TSVF), were also identified.

NUMERICAL STUDY

The experimental study presented in the previous section provided evidence that TSV could exist in tip flowfields. However, the discrepancies were from two aspects. One was that the difference between the measured and simulated frequency from single-passage unsteady simulation was relatively large. The other was the measured signals had the bandwidth on the order of 100 Hz, except for the uncertainties from measurements, signal processing, and non-physical reflections from the specified inlet and outlet boundaries in simulations. Moreover, there was no “tip clearance backflow” observed during stall inception process in previous single-passage unsteay simulations (Yanhui [18]). All theses inconsistencies indicated that whole-passage unsteady simulations must be conducted at near stall conditions so that the physical mechanisms behind the unsteady phenomena could be adequately explained.

Numerical schemes

Numerical simulations were performed by flow solver EURANUS. It computed the conservative Reynolds-averaged Navior-Stokes equations without *ad hoc* modeling of any flow phenomena other than models required for turbulence. The parallel version of this solver was implemented in a scalable form for using MPI message passing. The parallel implementation employed domain decomposition and supports general muti-block grids with arbitrary grid-block connectivity.

The equations were discretized in space using a cell-centered finite volume formulation. With a view to capture the tip leakage vortex sharply near the end-wall, a 2nd-order upwind scheme based on a flux difference splitting formulation (Roe, [19]) with the Van Albada limiter being implemented was chosen to evaluate the inviscid fluxes. The viscous fluxes were determined in a central differencing manner with Gauss’s theorem. For steady simulations, the equations was sloved using an explicit four-stage Runge-Kutta method with local time step to obtain steady-state solutions. For unsteady simulations, equations were solved using the implicit dual time-stepping method proposed by Jameson [20], which consists in adding to the time-dependent equations pseudo-time derivative terms. This methodology retains the main advantages of the explicit time integration scheme already implemented for resolving steady-state problems. One equation turbulence model of Spalart-Allmaras [21] was employed to estimate the eddy viscosity. Local time stepping, implicit residual smoothing and multi-grid techniques were used to reduce the computation cost.

Physical time step for unsteady simulations was determined by rotational speed, and it took a rotor blade 20 time steps to passing through one pitch. Within each physical time step, 50 pseudo time iterations with a CFL number of 2-3 were performed.

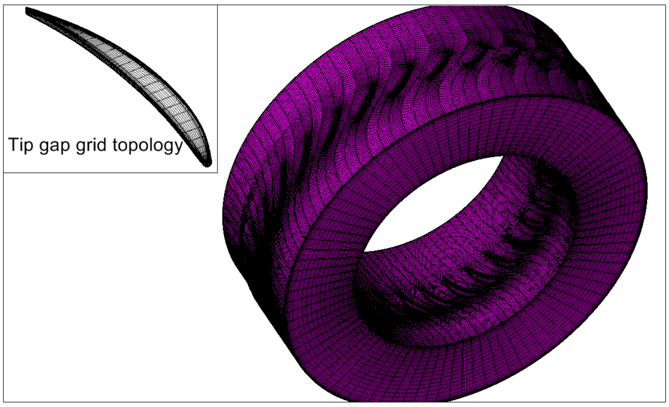

Figure 6 Computational mesh

Gridding

In the proper sense, the present study was the extension of numerical investigations conducted by Yanhui Wu [18], and the same single-passage grid should be adopted. However, limited by computation resources, another relatively coarse single-passage grid with true tip gap was built. To reduce the grid skewness, O4H topology was chosen to model the main flow region, and butterfly topology was used to model the true tip gap. This grid consisted of 57 points along the annulus height, including 17 point along the radial height of the tip gap, thus having locally fine grid spacing near casing. The minimum grid spacing on the solid wall was 5×10^{-6} to evaluate the viscous fluxes at the wall by applying the no-slip and adiabatic conditions. This minimum grid spacing gave $y^{+}\leq 3$ at the walls. The full-annulus grid was shown in Figure 6, which was generated by rotating and replicating the single-passage grid around the annulus. There were 30 blade passages for the entire grid with a total of 6,140,610 grid points, and the grid was partitioned into 210 blocks.

Boundary condition

No-slip and no-heat transfer conditions were imposed at solid boundaries. The flow was assumed to be steady-state at the inlet/outlet of the rotor. The flow angle, total pressure and total temperature were specified to be uniform across the whole inlet domain according to the experimental data. For steady calculations, the static pressure was set at the midspan, and the radial equilibrium equation was used to obtain the radial profile. Due to the substantial unsteadiness occurring at near stall conditions, the presetting pressure level at outlet boundary could not match the pressure variation arising from the unsteady flow. Therefore, the mass flow rate and initial static pressure were specified at outlet boundary for unsteady calculations, the successive pressure modification was calculated according to:

$$p^{new} = p^{old} + RELAXP\frac{\sqrt{\gamma_{gas}T_{ref}}}{L_{ref}^{2}}\left(Q^{actual} - Q^{imposed}\right)$$

Where L_{ref} and T_{ref} were the characteristic length and reference temperature, γ_{gas} and $RELAXP$ were the gas constant and relaxation factor, Q^{actual} and $Q^{imposed}$ were the mass flow rates calculated at the preceding time step, and specified at outlet boundary, P^{new} and p^{old} were the static pressures specified at the outlet boundary at the current and preceding time steps.

Results and discussion

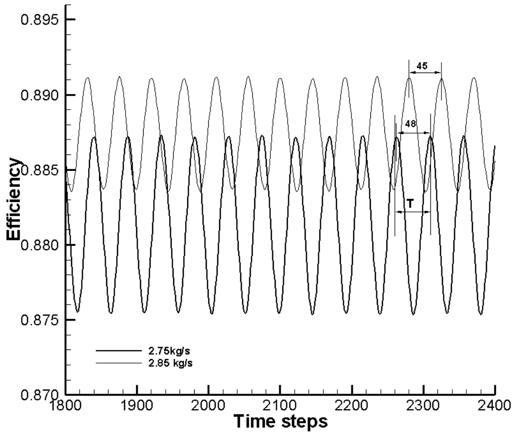

Figure 7 The comparison of efficiency histories between two operating conditions

The steady simulations were first carried out by gradually increasing the exit pressure till the last stable point was obtained. The preliminary analysis of the flow fields for the last stable point showed that the interface between the incoming and tip clearance flow was still in the blade passage. The interface between the incoming and tip clearance flow becoming parallel to the leading edge plane was a common feature of spike initiated stall, which was observed in measurement conducted by koach saathoff and stark [22] and in computation conducted by Vo [11]. Thus, the first unsteady simulation, where the initial solution was from the last stable point of steady simulations, was further conducted by presetting the mass flow rate at exit boundary. The time history showed the solution converged with nearly periodic fluctuation of the integrated properties, especially for efficiency and torque acting on the blade. Then, the calculations continued by reducing the outlet mass flow rate with the decrement of 0.05

kg/s. The last stable point for unsteady simulation was obtained at the flow condition with equivalent corrected mass flow rate of 2.75 kg/s.

Figure 7 compared the time history for flow condition with corrected mass flow rate of 2.85 kg/s with that of the last stable point from unsteady simulations. Generally speaking, the efficiency fluctuated with the period close to 50 time steps, i.e., 2.5 blade passing time, and the oscillation magnitude increased with the flow rate decreased. These phenomena were consistent with the pressure variation of monitor point on the pressure surface 30% axial chord downstream of the leading edge and 3 mm inboard of the blade tip (Yanhui wu [18]). However, if the time history was closely examined, the period of efficiency oscillation increased from 45 to 48 time steps with the mass flow rate decreased.

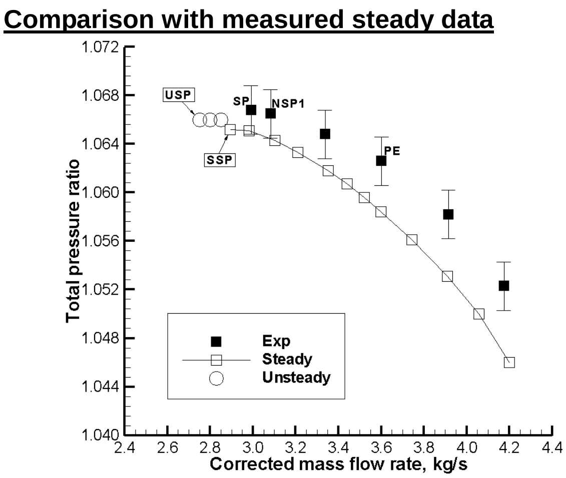

(a) Total pressure ratio

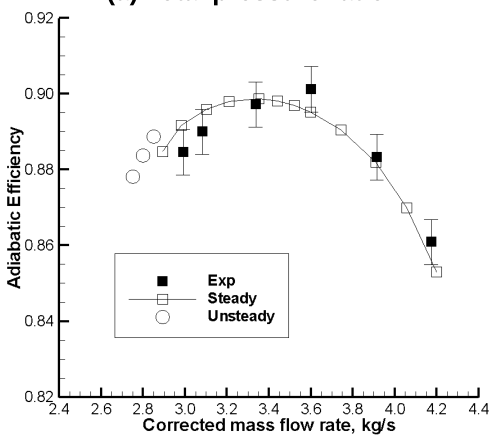

(b) Adiabatic efficiency

Figure 8 the comparison of predicted and experimental total performances

To validate the simulation results, the predicted results were first compared with the measured steady data. The comparison between the predicted and measured rotor performance was shown in Figure 8. The time-averaged data from unsteady simulations were also shown in this figure, where the last stable points from steady and unsteady simulations were marked by SSP and USP respectively. The overall shape matches the experiment's well. The deviation in total pressure ratio was significantly large at the choked end, but the predicted values fell into error band when approaching the stall end. The difference between SSP and SP is about 0.1 kg/s. This meant the steady simulation predicted the real stall point reasonably well as far as the measurement uncertainty was concerned. However, it seemed that the real stall point was over-predicted by unsteady simulations. The final pressure specified at outlet boundary for USP was examined, and it was found that the maximum pressure difference between USP and SSP was less than 150 Pa. The so small increment was hardly assured even if the throttle valve was finely adjusted.

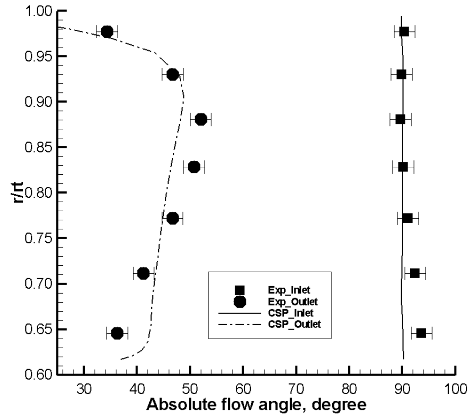

(a) Inlet/outlet absolute flow angle

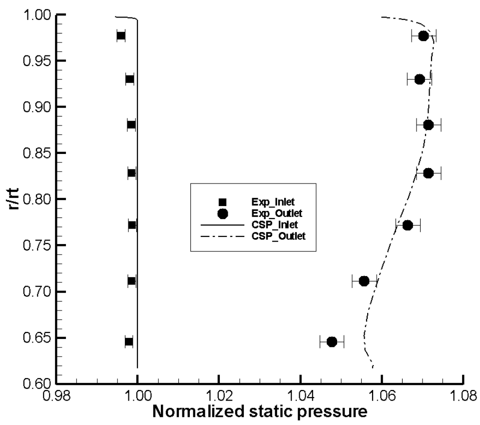

(b) Inlet/outlet total pressure

Figure 9 The comparisons of predicted and experimental elemental performances

Figure 9 compared the calculated spanwise profiles of total pressure and flow angle at SSP with those at SP. Generally, the numerical results reproduced the measured radial profiles of total pressure and flow angle well. Especially, the predicted values agreed much better with the measured data from casing to 90% span. The discrepancy between the predicted and measured profile from hub to 90% span was probably due to the difference between numerical and experimental inlet boundary condition. In experiments, the air flowed into the compressor through a radial-axial inlet duct, as shown in Figure 1. This led to the nonuniform distributions of inlet flow parameters along spanwise direction. The relatively larger flow angles compared to those from calculation indicated that initial negative swirl was exerted on the blade elements near hub, thus making them produce the lower experimental flow angle and total pressure at outlet plane. The flow redistribution due to the nonuniform inlet flow angle apparently contributed to the slightly high experimental outlet flow angle and total pressure around midspan.

The other major difference between the numerical and experimental setup was that it was assumed that all 30 rotor passages were identical, with a uniform clearance gap. However, the measurements showed a little variation in measured clearance gap between blade passages. This difference, as well as numerical schemes and turbulence model, contributed to the remainder of disagreements between measurements and calculations. However, the good agreement of flow distributions near casing provided the confidence in analyzing flow features of tip clearance flow using the numerically obtained flowfields.

Calculated unsteady characteristics at near stall conditions

Because the flow structures near casing from unsteady simulations were similar, the following only presented the results for USP. The analyses were made in the period of 50, denoted by T as shown in Figure 7, since the solutions were saved every five time steps.

To compare the predicted results with those reported by Yanhui Wu [18], particle traces issued at the first node away from blade tip were firstly examined. Figure 10 represented the instantaneous leakage streamlines in one tip passage during one period of efficiency fluctuation. For the subsequent analysis requirements, this figure also illustrated the spatial low-energy regions, which were confined by $W/Ut < 0.15$ (where W was the relative velocity and Ut is tip speed), and isolines of entropy at blade tip section, which were used to identify the interface between incoming flow and tip clearance flow (a red dashed line).

It was obvious that that tip leakage vortex (TLV) took on the bubble-type breakdown, which was same as that observed in steady simulations (Y. Wu et al. [17]). Apart from the breakdown of TLV, the most prominent feature in Figure 10 was the activity of tip secondary vortex (TSV). It appeared at t=5/50T, and then convected downstream along streamwise direction. At t=50/50T, TSV almost disappeared, but a new TSV near the leading edge and pressure side of passage started to appear. A new period of fluctuations thus initiated from this point. These observations were similar to those reported by Yanhui Wu [18], where the simulations were based on a fine mesh topology with total grid points about 1000,000. The similarity of the predicted results between the two sets of grid demonstrated the current relatively coarse mesh with locally fine grid around the blade tip had the capability for capturing the complicated flow structure near casing fairly well.

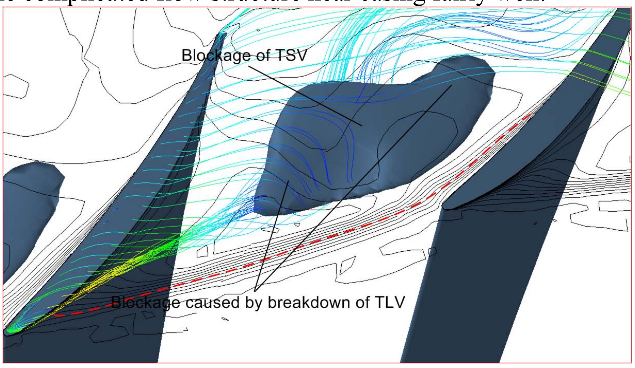

(a) t =10/50T

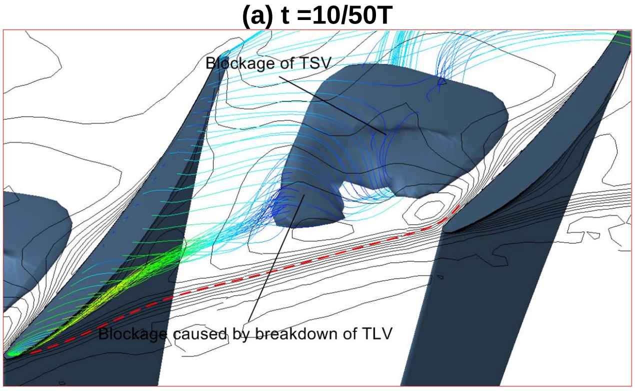

(b) t =20/50T

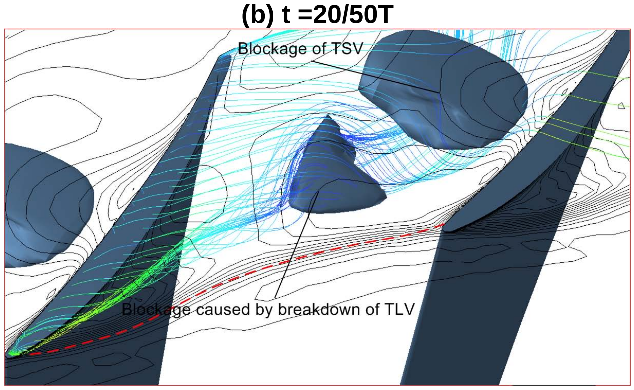

(c) t =30/50T

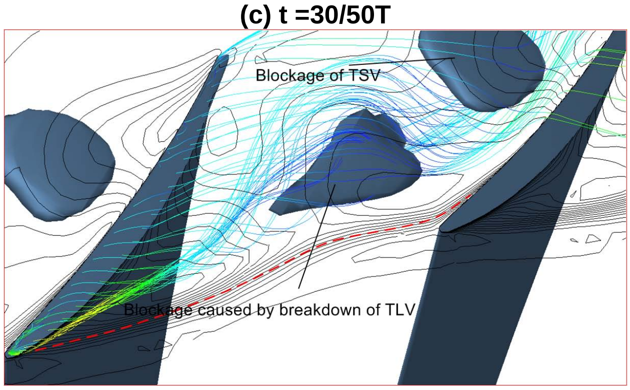

(e) t =40/50T

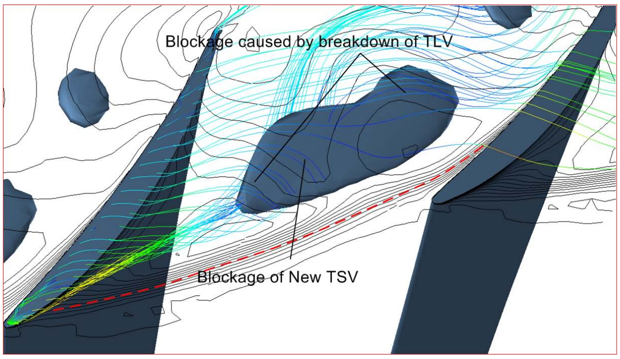

(f) t =50/50T

Figure 10 Instantaneous leakage streamlines during one period of efficiency fluctuation

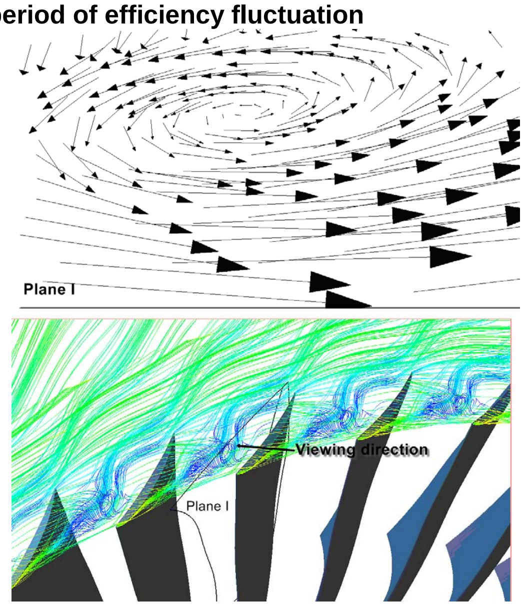

Figure 11 Instantaneous velocity vectors on a plane nearly vertical to the vortex core of TSV at t=20/50T

For better identifying the three-dimensional structure of TSV and its rotation direction, Figure 11 showed the velocity vector distribution on a plane, which was nearly perpendicular to the vortex core of TSV at t=20/50T. It was clearly seen that TSV formed just below the blade tip section, and propagated diagonally inward. The vortex core of TSV was nearly perpendicular to that of TLV. Due to its anti-clockwise rotation, it would induce a reverse flow region on the blade-to-blade section at blade tip.

Figure 12 presented the negative axial velocity distribution on a surface of revolution at the blade tip. A negative axial velocity region with narrow and long shape near the leading edge and suction side of passage arose from the motion of TLV. At different instants, the area of this negative region remained relatively same. Another negative axial velocity region, deduced from its locations and shape, was caused by TSV. In contrast to the reverse flow region caused by TLV, its area varied at different instants. As it rolled downstream along the pressure side of the passage with enlarging area, the interface between incoming and tip clearance flow was pushed forward and reached the leading edge plane (Figure 10b-c). Then, it gradually returned back into the passage as the negative axial velocity region induced by TSV diminished.

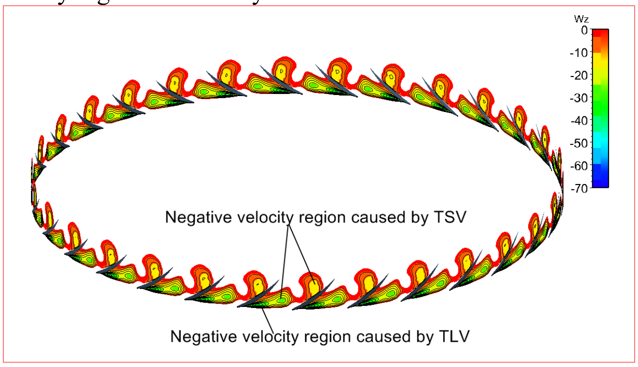

(a) t=10/50T

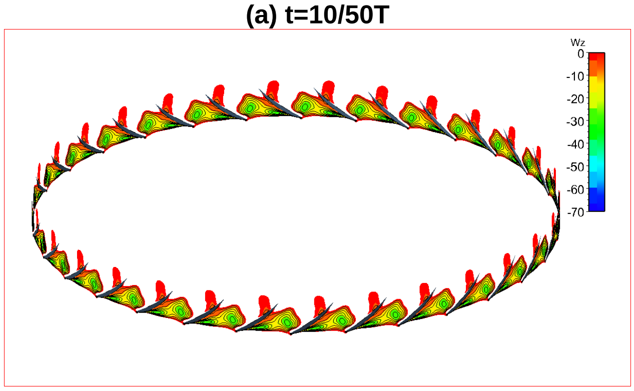

(b) t=20/50T

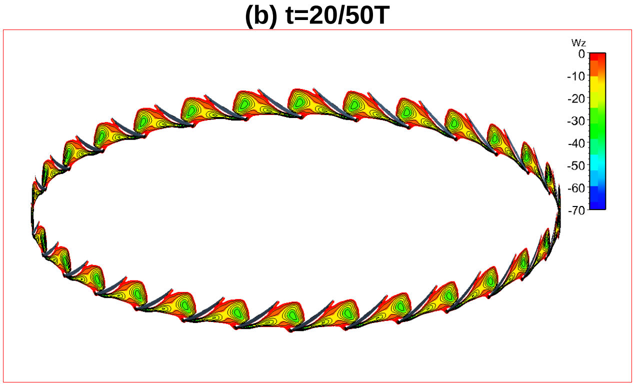

(c) t=30/50T

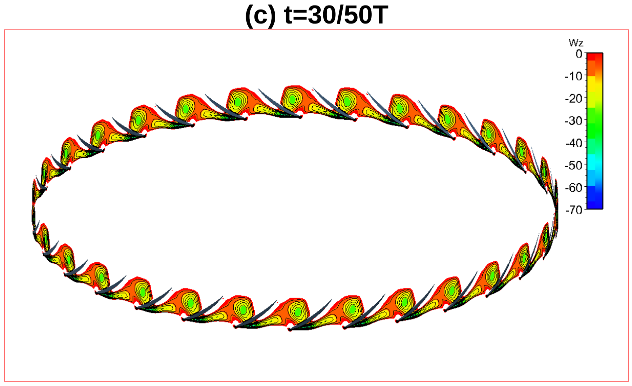

(d) t=40/50T

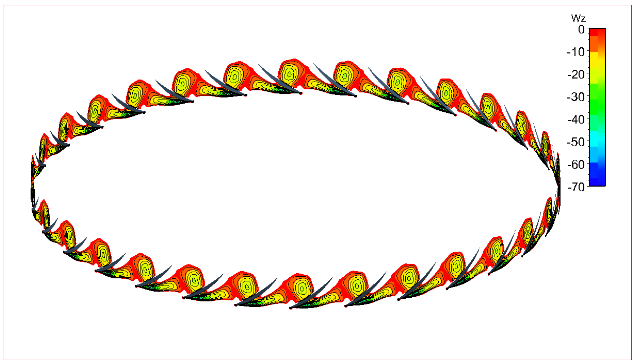

(e) t=50/50T

Figure 12 Instantaneous negative axial velocity distributions during one period of efficiency fluctuation

Due to the fact that the formation of TSV was so complicated that there was no proper parameter that could quantify its strength. However, changes in the spatial low-energy region associated with the motion of TSV (Figure 10), along with the negative axial velocity region induced by TSV on the blade-tip section (Figure 12), suggested that the intensity of TSV underwent a “weak-strong-weak” variation process during one period of efficiency fluctuation. It was obvious that TSV had the more strength at t=20/50T and 30/50T. The larger blockage effect arising from the stronger TSV was responsible for the forward movement of interface between incoming and tip clearance flow.

As shown in Figure 12, the whole-passage simulation showed no significant periodic variation of flow properties across passages so that the activities of TSV in all passages were almost in-phases. Hence, the active period of TSV was consistent with that of efficiency. At t=25/50T, the TSV had approximated to its most strength, so efficiency reached its minimum value due to the maximum loss caused by TSV. At instant t=50/50T, the TSV almost disappeared in the rear part of passage, while an embryonic TSV started to occur, thus bringing the efficiency to its maximum value. Consequently, the movement of TSV is the main causes of the unsteadiness in flowfields near casing at near stall conditions.

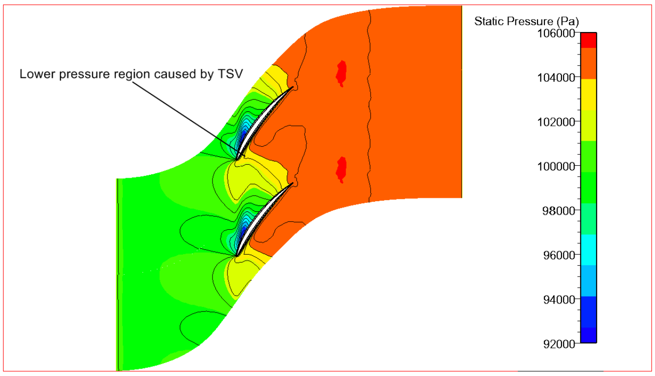

(a) t=10/50T

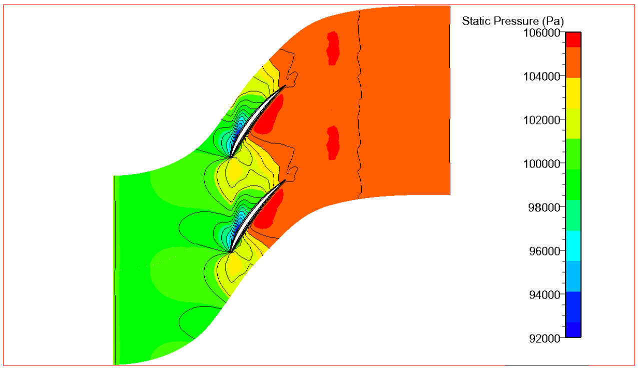

(b) t=20/50T

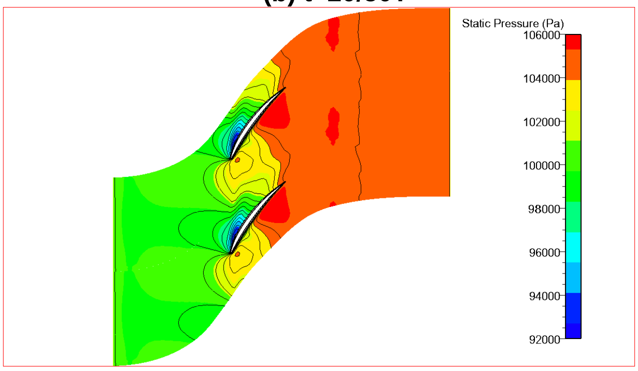

(c) t=30/50T

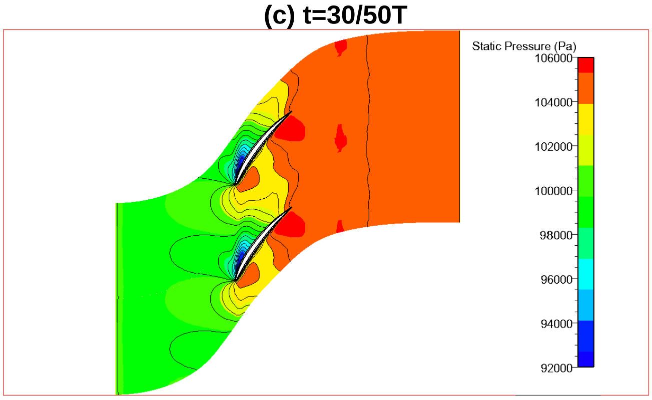

(d) t=40/50T

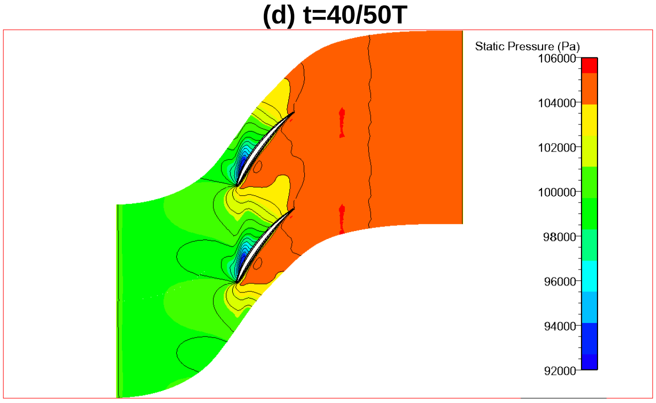

(e) t=50/50T

Figure 13 Instantaneous static pressure distributions during one period of efficiency fluctuation

The activity of TSV in near-tip passage would influence the pressure distributions on casing. Figure 13 represented the instantaneous static pressure distributions on the casing in the same rotor passage as that shown in Figure 10. In contrast to the results shown in Figures 10 and 12, the pressure oscillations on the casing, especially near the pressure side of blade passage, was closely related to the motion of TSV. As compared to the other part of TSV, its front end was very close to the casing. Hence, a low pressure region located near the pressure side of passage appeared due to its spiral motion. The stronger TSV had, the lower pressure it induced. For example, a spot with even low static pressure, though hardly perceived, occurred at t=20/50T and 30/50T. At t=30/50T, a very small high pressure spot (red color) appeared near the leading edge and pressure side of passage due to the recovery of diffusion process in near-tip passage. This high pressure spot enlarged with the rearward movement of TSV. Finally, it merged into the high pressure region located near the outlet of rotor passage accompanied by the disappearance of low pressure region induced by the front end of TSV at t=50/50T.

The above pressure oscillations on casing indicated that the high-frequency transducer mounted on the casing could detect a signal with the frequency equaling to that of TSV on condition that TSV was in activity synchronously in all passages. As shown in Figure 7, the period of efficiency fluctuation at flow condition with corrected mass flow rate of 2.85 kg/s was 45 time steps. That is, the active frequency of TSV was 1806 Hz at this flow condition. The power density of the characteristic hump shown in Figure 5 decreased along chordwise direction, and this was consistent with the "weak-strong-weak" variation process of TSV during one unsteady cycle. Therefore, the occurrence of this hump most probably attributed to the movement of TSV due to the fact the flow condition with corrected mass flow rate of 2.85 kg/s was very close to the measured stall point (SP).

Flow mechanism associated with the formation of TSV

In order to explore the origin of TSV, the numerically obtained flowfields were further explored. Figure 14 presented the typical streamlines, which contributed to the formation of TSV, at three representative instants, and the corresponding near-tip loading during one unsteady cycle of TSV, was shown in Figure 15. In conjunction with Figures 10, 14 and 15, it could be seen:

At t=10/50T, it was the low energy leakage fluid from two adjacent passages, not exclusive of those from the other adjacent passages (not shown in Figure 14(a)), were rolled into TSV. They turned direction when encountering the interface between incoming and tip clearance flow, and interact with the lower-energy region caused by the breakdown of TLV, thus forming TSV. The spatial lower-energy region due to the motion of TSV was embedded into the low-energy region caused by the breakdown of TLV.

At t=20/50T, a pressure trough appeared on the pressure distribution of pressure side corresponded to the front end of TSV. The tip loading near leading edge decreased due to the presence of this trough, thus decreasing the strength of TLV. The lower-energy region caused by the breakdown of TLV contracted accordingly. Meanwhile, the pressure difference around the mid-rear chord increased. This forced the more low energy fluid leak through gap from this fraction of tip chord, and roll into TSV, hence increasing the strength of TSV. At the same time, the low energy fluid due to the separation of blade suction boundary layer were also rolled into TSV with its rear end approaching the separation line, thus further increasing the strength of TSV. As a result, the low-energy region associated with the motion of TSV increased rapidly. It started to be detached from the low-energy region cause by the breakdown of TLV with the rearward movement of TSV.

At t=30/50T, the low-energy region caused by the breakdown of TLV expanded slightly with the recovery of tip loading around the leading edge. As TSV further moved rearward, the two low-energy regions were totally separated, thus forming a low-loss path in near-tip passage. Although the tip loading in the rear part of chord was almost same as that at t=20/50T, the strength of TSV decreased because most of the leakage fluid from the rear part of chord flowed into the next passage through the low-loss path, and the low-energy region due to the motion of TSV diminishes accordingly. The low-energy fluid due to the separation of suction boundary layer was still able to roll into TSV at this moment.

After t=30/50T, TSV was not capable of rolling up the low-energy fluid from the separation of boundary layer into it, and it went into a self-dissipation process. With the further rearward movement of TSV, the loading in the fore part of tip chord gradually increased, thus leading to the progressive expansion of low-energy region arising from the breakdown of TLV. At t=50/50T, the tip loading was nearly restored to its original state, and a new TSV hence appeared.

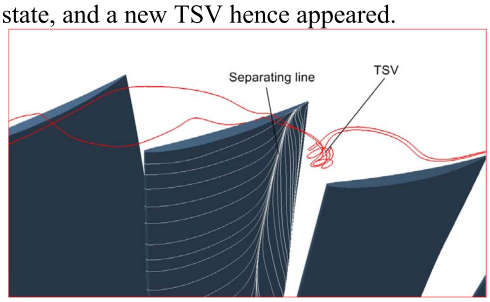

(a) t=10/50T

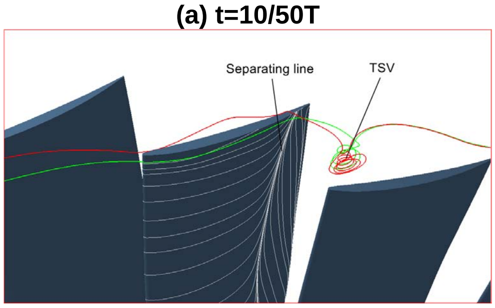

(b) t=20/50

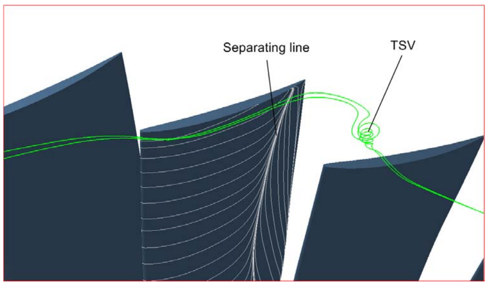

(c) t=30/50T

Figure 14 Typical streamlines rolled into TSV at three representative instants during one unsteady cycle

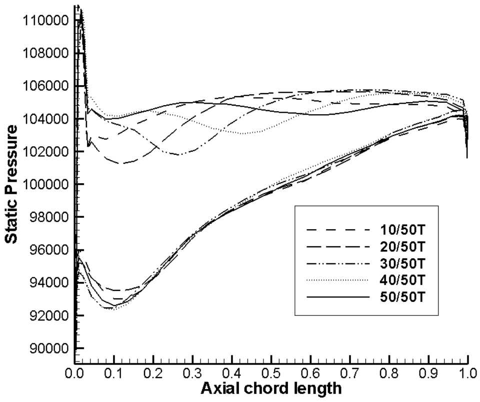

Figure 15 Instantaneous near-tip loading variations during one unsteady cycle of TSV

In summary, the interaction of the low-energy leakage fluid from adjacent passages with the broken-downed TLV was the flow mechanism for the formation of TSV. Once TSV appeared in tip flowfields, its rearward movement would lead to a periodic variation in near-tip blade loading, which in turn altered the strength of TLV and TSV, accordingly the low-energy regions associated with the breakdown of TLV and the motion of TSV. Thus, a self-sustained unsteady flow oscillation in tip flowfields was set up.

IMPLICATIONS FROM CURRENT INVESTIGATIONS

From experimental and numerical investigations, it can be inferred:

(1) The strength of TSV will increase due to the increase in near-tip loading and the severe boundary separation with mass flow rate decreased. This will lengthen the self-dissipation process of TSV, and accordingly the active period of TSV, as shown in Figure 7.

(2) The hump with bandwidth on the order of 100 HZ in experiments may be due to the severe loss of periodic flow across passages as compared to that observed in simulation (Figure 12). Hence, the transducer mounted on the casing will detect the pressure oscillations due to the movement of TSV with distinctive period in different tip passages.

CONCLUDING REMARK

In order to investigate the pre-stall behavior of an axial flow compressor rotor, which was experimentally observed with spike-type stall inception, systematical experimental and whole-passage simulations were laid out to analyze the internal flow fields in the test rotor. In this part, emphases were put on the analyses of experimental results and the predicted results from steady simulations and unsteady simulations which converged to equilibrium solutions with nearly periodic fluctuations of efficiency. The following conclusions were drawn:

1) Overall shape of predicted total characteristics matched the experiment's well. Spanwise distributions of aerodynamic parameters, especially near casing, also agreed well with the experimental data. These provided the confidence in analyzing the flow features of tip clearance flow using numerically obtained flowfields.
2) Through analyzing the instantaneous flow structure near rotor tip at near stall conditions, it was found that TSV, which appeared in the previous unsteady single-passage simulations, did exist in tip flowfields of whole-passage simulations. The cyclical motion of this vortex was the main source of the nearly periodic variation of efficiency.
3) The simulated active period of TSV increased with mass flow rate decreased to the last stable point from unsteady simulations. The simulated frequency of TSV at flow condition very close to the measured stall point equaled to the frequency of characteristic hump identified from the instantaneous casing pressure measurements, and this implied the occurrence of this hump was most probably due to the movement of TSV.
4) Further flowfield analyses indicated the interaction of the low-energy leakage fluid from adjacent passages with the broken-downed TLV was the flow mechanism for the formation of TSV. Once TSV appeared in tip flowfields, its rearward movement would lead to a periodic variation in near-tip blade loading, which in turn altered the strength of TLV and TSV, accordingly the low-energy regions associated with the breakdown of TLV and the motion of TSV, thus establishing a self-sustained unsteady flow oscillation in tip flowfields.

ACKNOWLEDGMENTS

The authors would like to acknowledge the supports of National Natural Science Foundation of China, Grant No. 51076133, and the support of NPU Foundation for Fundamental Research, Grant No. W018101, and the support of Aeronautic Science Foundation, Granted No. 2010ZB53016.

REFERENCES

[1] Inoue, M., Kuroumaru, M., and Fukuhara, M., 1986, "Behavior of Tip Leakage Flow Behind an Axial Compressor Rotor," ASME Journal of Engineering for Gas Turbines and Power, Vol. 108, No. 1, pp. 7-14.

[2] Inoue, M., and Kuroumaru, M., 1989, “Structure of Tip Clearance Flow in an Isolated Axial Compressor Rotor,” ASME Journal of Turbomachinery, Vol. 111, No. 3, pp. 250-256..

[3] Inoue, M., Kuroumaru, M., and Ando, Y., 1990, “Behavior of Tip Clearance Flow in Axial Flow Impellers at Low Flow Rate”Proceedings of the 3rd Japan-China Joint Conference on Fluid Machinery, Vol. II, pp. 179-186.

[4] Inoue, M., Kuroumaru, M., Iwamoto, T., and Ando, Y., 1991, “Detection of a Rotating Stall Precursor in Isolated Axial Flow Compressor Rotors,” ASME Journal of Turbomachinery, Vol. 113, No. 2, pp. 281-289.

[5] Furukawa M, Inoue M, Saiki K, et al. The role of tip leakage vortex breakdown in compressor rotor aerodynamics. ASME Journal of Turbomachinery, 1999, 121(3): 469-480.

[6] Baojie, L., Xianjun, Y., Hongwei, W., Huoxing, L. etc, 2004, “Evolution of the Tip Leakage Vortex in an Axial Compressor Rotor”, ASME-2004-53703.

[7] Furukawa M, Saiki K, Yamada K, et al. Unsteady flow behavior due to breakdown of tip leakage vortex in an axial compressor rotor at near-stall condition. ASME Paper, 2000-GT-666, 2000

[8] Yamada K, Furukawa M, Nakano K Unsteady three-dimensional flow phenomena due to breakdown of tip leakage vortex in a transonic axial compressor rotor. ASME Paper, 2004-GT-53745, 2004

[9] März, J., Hah, C., and Neise, W. An Experimental and Numerical Investigation into the Mechanisms of Rotating Instability, ASME Journal of Turbomachinery, 2002, 124:367~375

[10] Hoying D A, Tan C S, Vo H D, et al. Role of blade passage flow structures in axial compressor rotating stall inception[J]. ASME Journal of Turbomachinery, 1999, 121(4): 735-742

[11] Vo H, Greitzer E M. Criteria for spike initiated rotating stall. ASME Paper, GT2005-68374, 2005.

[12] Hah C, Bergner J, Schiffer H., Short length-scale rotating stall inception in a transonic axial compressor-criteria and mechanism[R]. ASME Paper, GT2006-90045, 2006.

[13] Jen-ping C., Michael D. H., Pre-stall Behavior of a Transonic Axial Compressor Stage via Time-Accurate Numerical Simulation. ASME Paper, GT2007-27926.

[14] Xingen Lu, Wuli Chu, Junqiang Zhu. Numerical Investigations of the Coupled Flow through a Subsonic Compressor Rotor and Axial Skewed Slot. ASME Journal of Turbomachinery, 2007.

[15] Yanhui Wu, Wuli Chu, Haoguang Zhang. Parametric Investigation of Circumferential Grooves on Compressor Rotor Performance”. ASME Journal of Fluids Engineering, 2010.

[16] Lu Xingeng, 2007, “Flow Instability and its Passive Control Strategies in Axial-flow Compressor,” PH.D. Thesis, Northerwestern Polytechical University.

[17] Yanhui Wu, and Wuli, Chu., 2006, “Behavior of tip clearance flow in an axial flow compressor rotor”, ASME Paper GT2006-90399.

[18] Yanhui Wu, Qingpeng Li, Wuli Chu. Numerical Investigation into Unsteady Behavior of Tip Clearance Flow and its possible link with stall inception. Proceedings of the Institution of Mechanical Engineers Part A-Journal of Power and Energy, 2009.

[19] Roe, P. L., 1981, “Approximate Riemann Solvers, Parameter Vectors and Difference Schemes”, Journal of Computation Physics, Vol. 43, pp. 357-382.

[20] Jameson, A., 1991, “Time-dependent calculations using multigrid, with application to unsteady flows past airfoils and wings”, AIAA-Paper 91-1596.

[21] Spalart, P. R., and Allmaras, S. R., 1992, “A one Equation Turbulence Model for Aerodynamic Flows,” AIAA 92-0439.

[22] Saathoff , H. and Stark, U., 2000, “Tip clearance Flow Induced Endwall Boundary Layer Separation in a Single-Stage Axial-Flow Low-Speed Compressor”, ASME Paper 2000-GT-0501.